




Cite this: *RSC Adv.*, 2023, 13, 27923

# Fabrication of inverse opal molybdenum sulfide and its use as a catalyst for H<sub>2</sub> evolution†

Thai D. Nguyen,<sup>a</sup> Huong T. L. Phung,<sup>ab</sup> Duc N. Nguyen,<sup>a</sup> Anh D. Nguyen <sup>\*a</sup> and Phong D. Tran <sup>\*a</sup>

Amorphous molybdenum sulfide (MoS<sub>x</sub>) and crystalline molybdenum disulfide (MoS<sub>2</sub>) are attractive noble-metal-free electrocatalysts for the H<sub>2</sub> evolution reaction from water. Their actual activities depend on the quantity of active sites which are exposed to the electrolyte, which in turn, is influenced by their specific electrochemical surface area. Herein we report on the fabrication of regular inverse opal MoS<sub>x</sub> and MoS<sub>2</sub> films by employing polystyrene nanoparticles with diameters in the range of 30–90 nm as hard templates. The use of these catalysts for the H<sub>2</sub> evolution reaction in an acidic electrolyte solution is also presented. Impacts of the regular porous structure, the film thickness as well as the chemical nature of the catalyst (MoS<sub>2</sub> versus MoS<sub>x</sub>) are discussed. It shows a catalytically-effective-thickness of ca. 300 nm where the electrolyte can fully penetrate the catalyst macropores, thus all the catalytic active sites can be exposed to the electrolyte to achieve the maximal catalytic operation.

Received 5th May 2023  
Accepted 6th September 2023

DOI: 10.1039/d3ra02972g

rsc.li/rsc-advances

## Introduction

Water splitting is an attractive technology for the large-scale production of green H<sub>2</sub>.<sup>1</sup> It consists of two half reactions, namely the hydrogen evolution reaction (2H<sup>+</sup> + 2e<sup>−</sup> → H<sub>2</sub>) and the oxygen evolution reaction (2H<sub>2</sub>O → O<sub>2</sub> + 4H<sup>+</sup> + 4e<sup>−</sup>). Because these reactions require multiple electrons and multiple protons, they have slow kinetics. Between the two, the hydrogen evolution reaction (HER) has faster kinetics in comparison to the oxygen evolution reaction (OER).<sup>2</sup> Nevertheless, an efficient electrocatalyst is still indispensable to realize large scale H<sub>2</sub> production with moderate overpotentials.<sup>3</sup> A prime candidate for this role is platinum (Pt), which requires almost zero overpotential to operate in an acidic electrolyte solution.<sup>4</sup> However, the rarity of Pt on the Earth's crust hinders its application in industry, where large-scale production of H<sub>2</sub> is demanded. Thus, great efforts have been mobilized to search for alternative catalysts made of Earth-abundant-elements to replace Pt-based ones.<sup>4b,5</sup> To date, the amorphous non-stoichiometric molybdenum sulfide (denoted hereafter as MoS<sub>x</sub>) and the crystalline molybdenum disulfide (denote hereafter as MoS<sub>2</sub>) are known to be among the most promising alternatives to Pt. Substantial information on the H<sub>2</sub> evolution mechanism on MoS<sub>x</sub> (ref. 5d and 6) and MoS<sub>2</sub> (ref. 4b and 7) has been obtained,

promoting the identification of appropriate strategies for further boosting the performance of these catalysts. Since the H<sub>2</sub> evolution reaction occurs on the Mo center, creating a S-vacancy is a valuable strategy to boost the catalytic activity of MoS<sub>2</sub>. It could be realized either by electrochemical oxidation<sup>8</sup> or plasma treatment.<sup>9</sup> Introducing another transition metal such as Co is also an efficient strategy to activate the S<sup>2−</sup> or (S−S)<sup>2−</sup> centers, which possess almost negligible catalytic activity, thus promoting the overall performance of MoS<sub>2</sub> and MoS<sub>x</sub> catalysts.<sup>10</sup> As nanocatalysts, the catalytic activities of MoS<sub>2</sub> and MoS<sub>x</sub> could be tuned by varying their particle shape and size.<sup>11</sup> In principle, the smaller the particle is, the larger the specific surface area will be, thus higher population of active centers on the particle's surface will be available and exposed to the electrolyte. As the result, higher catalytic activity could be expected. Indeed, it was demonstrated that by decreasing the size of the MoS<sub>2</sub> crystals, the density of active sites located on the MoS<sub>2</sub> edges increased, leading to a significant boost in catalytic activity.<sup>11a,b</sup> Nevertheless, it is challenging to fabricate small nanoparticles, *e.g.* having diameter of less than 10 nm, with a narrow size distribution. Moreover, agglomeration of small nanoparticles when they are deposited onto the electrode surface for catalysis operation is a serious problem leading to reduction of the specific surface area.

In this context, the engineering of microporous regular three-dimensional (3D) catalyst appears to be an attractive strategy to maximize the catalyst's specific electrochemical surface area, thus maximizing the population of active sites exposed to the electrolyte. Through this process, the catalytic activity of the material can be boosted without negative impact to the robustness. In general, the preparation of regular 3D

<sup>a</sup>University of Science and Technology of Hanoi, Vietnam Academy of Science and Technology, 18 Hoang Quoc Viet, Hanoi, Vietnam. E-mail: [nguyen-duc.anh@usth.edu.vn](mailto:nguyen-duc.anh@usth.edu.vn); [tran-dinh.phong@usth.edu.vn](mailto:tran-dinh.phong@usth.edu.vn)

<sup>b</sup>Graduated University of Science and Technology, Vietnam Academy of Science and Technology, 18 Hoang Quoc Viet, Hanoi, Vietnam

† Electronic supplementary information (ESI) available. See DOI: <https://doi.org/10.1039/d3ra02972g>



nanomaterials can be classified into soft-templating, hard-templating and template-free preparation methods.<sup>12</sup> The template-free and soft-templating methods are normally lack of controllability and uniformity, thus are not appropriate for engineering a stable and uniform structure.<sup>12a</sup> On the other hand, the hard-templating method is rather technically complicated due to the strict requirement of a post-treatment step namely the removal of the hard template such as silica or polymers. In compensation for the complicated processing, the hard-templating method could offer well-ordered structures.<sup>13</sup> Using the hard-templating method, Kibsgaard *et al.*<sup>14</sup> presented a pioneer work fabricating mesoporous  $\text{MoS}_2$  with a double-gyroid morphology using a double-gyroid silica hard template. Therein, the Mo metal which had been electrodeposited within the silica host underwent sulfidation using  $\text{H}_2\text{S}$  gas, turning into  $\text{MoS}_2$ .<sup>14</sup> The silica was chemically etched out by a HF solution, generating the 3D- $\text{MoS}_2$ . In a 0.5 M  $\text{H}_2\text{SO}_4$  electrolyte solution, the 3D- $\text{MoS}_2$  catalyst generated a benchmarking catalytic current density of  $10 \text{ mA cm}^{-2}$  at an applied potential of  $-280 \text{ mV}$  versus the Reversible Hydrogen Electrode (RHE). Deng *et al.* reported on the preparation of  $\text{MoS}_2$  foam using  $\text{SiO}_2$  nanosphere as template, with  $(\text{NH}_4)_6\text{Mo}_7\text{O}_{24}$  and  $\text{CS}_2$  as precursors for Mo and S, respectively.<sup>15</sup> After etching out the  $\text{SiO}_2$  template,  $\text{MoS}_2$  foam nanoparticles having an average pore size of  $\sim 30 \text{ nm}$  was obtained. These nanoparticles were then drop-casted onto a glassy carbon electrode using Nafion polymer as the binder to enhance the stability of the catalyst layer. To generate the catalytic current of  $10 \text{ mA cm}^{-2}$ , this  $\text{MoS}_2$ -coated glassy carbon electrode required an applied potential of  $-210 \text{ mV}$  vs. RHE. Pumera *et al.* demonstrated the use of commercial polystyrene beads (hereafter referred as PS) coated on indium tin oxide (ITO) electrode surface as a template for preparing the microporous amorphous molybdenum sulfide  $\text{MoS}_x$ .<sup>16</sup> Therein, the  $\text{MoS}_x$  material was fabricated around the template *via* electrodeposition using an  $(\text{NH}_4)_2[\text{MoS}_4]$

deposition bath. When PS particles with diameter of  $3 \mu\text{m}$  or larger was used, only a sub-monolayer of PS particles was obtained, resulting in the deposition of a  $\text{MoS}_x$  film with rather low density. Denser  $\text{MoS}_x$  film was obtained using multiple layers of PS particles with smaller size, being  $0.24 \mu\text{m}$  in diameter. In an acidic electrolyte, namely 0.5 M  $\text{H}_2\text{SO}_4$  solution, the resultant 3D- $\text{MoS}_x$  required a potential of  $-240 \text{ mV}$  to sustain a catalytic current density of  $10 \text{ mA cm}^{-2}$ . The same approach has been exploited to engineer 3D- $\text{MoSe}_x$  catalysts using a deposition bath constituted of  $\text{H}_2\text{MoO}_4$  and  $\text{SeO}_2$  in 0.2 M  $\text{NH}_4\text{OH}$ .<sup>17</sup> It was found that the resultant  $\text{MoSe}_x$  was less hydrophobic and thus more catalytically active for the HER when the PS beads used as template are smaller in size.

Being inspired by this concept, by using smaller synthetic PS beads template, we aim to fabricate 3D- $\text{MoS}_x$  and 3D- $\text{MoS}_2$  matrix which have regular structure with higher number of material layers, and thus, higher material density. Fig. 1 schematically illustrates the preparation process that has been developed in this work for preparation of 3D- $\text{MoS}_x$  and 3D- $\text{MoS}_2$  matrix.

## Experimental methods

### Materials

Potassium persulfate (KPS) (99%), sodium dodecyl sulfate (SDS) (98%), styrene (99%) contained anti-polymerizer *t*-butyl catechol,  $\text{LiClO}_4$  95%,  $(\text{NH}_4)_2\text{MoS}_4$  99.97%,  $\text{CuSO}_4$  99%,  $\text{H}_2\text{SO}_4$  98% were purchased from Sigma-Aldrich. Prior to use, the styrene was treated with 10% sodium hydroxide solution in a separatory funnel three times in order to remove the anti-polymerizer.

### Synthesis of spherical polystyrene particles

The polystyrene spherical nanoparticles were synthesized using an emulsion polymerization method described by Yang *et al.*<sup>18</sup> In a typical experiment, SDS and KPS was dissolved in deionized

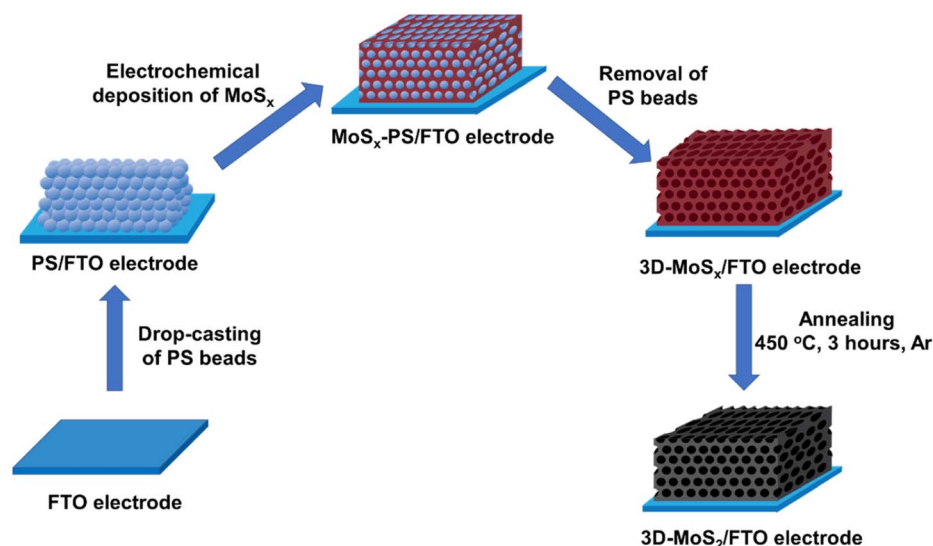


Fig. 1 Presentation of the stepwise fabrication process used for the preparation of 3D- $\text{MoS}_x$  and 3D- $\text{MoS}_2$  films on fluorine-doped tin oxide substrate.



water in a 100 mL round-bottomed flask equipped with a magnetic stirrer and a rubber septum. A defined amount of styrene was added and the mixture was vigorously stirred for 15 minutes while an  $N_2$  gas flow was aerated into the emulsion to remove dissolved  $O_2$ . The system was then kept at 70 °C for 24 hours to obtain complete polymerization. The PS nano-beads were collected as suspension and stored at ambient conditions. PS beads with diameter under 100 nm can be fabricated by variation of SDS/styrene weight ratio (Table S1†).

### Synthesis of 3D-MoS<sub>x</sub>

The 3D-nanostructured MoS<sub>x</sub> was electrochemically prepared on FTO-coated glass slides using chronoamperometry in aqueous solution with optimized parameters.<sup>19</sup>

**Preparation of PS/FTO working electrodes.** Prior to use, the commercially available FTO sheet was cut into a series of smaller pieces with dimensions of 1 × 2 cm. Electrically insulating thermal tape was used to prevent the connectors of the potentiostat from contacting with the electrolyte, as well as to define an area of 0.283 cm<sup>2</sup> as the active FTO electrode surface to be used for electrodeposition. The polystyrene beads were deposited on the electrode surface by drop-casting 50 μL of the polystyrene colloidal solution dispersed in water with concentration of 4 mg mL<sup>-1</sup>. The electrode was then dried at room temperature for 3 hours followed by vacuum drying at 10 mbar resulting in a polystyrene coated FTO electrode.

**Synthesis of 3D-MoS<sub>x</sub>.** The electrode was then immersed in the (NH<sub>4</sub>)<sub>2</sub>MoS<sub>4</sub><sup>20</sup> electrolyte solution as the working electrode in a conventional three electrodes setup. Ag/AgCl/KCl 3 M and Pt were used as reference and counter electrodes, respectively. In order to electrochemically grow MoS<sub>x</sub>, a potential of 0.4 V vs. NHE was applied on the working electrode until the desired amount of electrical charges has been transferred. After rinsing gently with DI water, the 3D-MoS<sub>x</sub> films were finally obtained by the dissolution of the polystyrene beads template by immersing the electrode in dichloromethane for 2 hours. For complete removal of the PS template, this treatment was repeated 5 times with fresh dichloromethane.

### Synthesis of MoS<sub>2</sub>

The previously prepared 3D-MoS<sub>x</sub> was converted into 3D-MoS<sub>2</sub> by an annealing process under a continuous flow of Ar using a Nabertherm RSH 50/500/13 tube furnace. The temperature ramping rate was kept at 10 °C min<sup>-1</sup> from room temperature to 450 °C. The furnace was then held at 450 °C for 3 hours and was cooled down naturally to room temperature.

### Materials characterization

Surface morphology analysis and cross-section imaging of the PS/FTO electrodes, MoS<sub>x</sub>, 3D-MoS<sub>x</sub> and 3D-MoS<sub>2</sub> films were performed by a field emission scanning electron microscopy (FE-SEM, Hitachi S4800, Japan) operated at 5 kV. For the SEM cross-section imaging, the back side of the 3D-MoS<sub>x</sub> and 3D-MoS<sub>2</sub> deposited FTO electrodes were cut by a diamond tip glass cutter following a line going through the middle of the piece. The electrode was then broken into two pieces by applying

pressure along the cutting line. SEM images were then collected in different positions on the freshly-exposed edge. Raman spectra were collected by using a LabRAM HR Evolution Raman Microscope (Horiba). Excitation was made by a green 532 nm laser with low power of 0.1 mW to avoid the MoS<sub>x</sub>-to-MoS<sub>2</sub> crystallization.<sup>21</sup> Size distribution of spherical PS particles have been analyzed employing dynamic laser scattering method using a Horiba SZ-100. Samples were diluted to the concentration of 1 mg mL<sup>-1</sup> and measured 3 times using 173° back-scatter (NIBS standard), the DLS signals were collected in 120 seconds for each measurement. The water contact angle measurement was assayed using H<sub>2</sub>SO<sub>4</sub> 0.5 M solution on a Kruss DSA25 drop shape analyzer.

### Electrochemical measurement and catalytic assay

Electrochemical properties and catalytic activities of the MoS<sub>x</sub> and 3D-MoS<sub>x</sub> were assayed in a 0.5 M H<sub>2</sub>SO<sub>4</sub> (pH 0.6) electrolyte solution. A conventional three electrode configuration was used with MoS<sub>x</sub> coated FTO as the working electrode, Ag/AgCl/3 M KCl as the reference electrode and a Pt wire as the counter electrode. Prior to measurement, the electrolyte solution was purged with N<sub>2</sub> for 30 minutes to remove dissolved dioxygen. Linear sweep voltammetry analysis was conducted using a Bio-Logic SP-300 potentiostat in the potential range from 0 to -0.4 V vs. RHE with a slow potential scan rate of 5 mV s<sup>-1</sup>.

EIS analysis of the samples was assayed in 0.5 M H<sub>2</sub>SO<sub>4</sub> (pH 0.6) electrolyte solution. Prior to EIS, the samples were assayed for 10 LSV scans from 0 to -0.4 V vs. RHE to reach the steady state of catalytic activity. The EIS was conducted at applied potential of -0.3 V vs. RHE over the frequency range from 100 000 kHz to 100 000 MHz, the AC probe amplitude was 10 mV.

## Results and discussions

### Fabrication of 3D-MoS<sub>x</sub> material

To the best of our knowledge, the commercially available PS nanoparticles are rather big, *e.g.* with average diameter of few hundreds of nanometers at the very least. Using big PS nanoparticle template would lead to a large volume of space within the catalyst film when the PS template is removed, thus resulting in a low catalyst loading. Herein, aiming to maximize the catalyst loading, we decided to prepare smaller PS nanoparticles with an average diameter ranging from 35 to 90 nm. To this end, the emulsion polymerization of styrene in water with the presence of potassium persulfate (KPS) initiator and sodium dodecyl sulfate (SDS) surfactant was employed (see ESI† for more details). We varied the SDS concentration in pure water to tune the average PS particle size (Table S1†).<sup>22</sup> Indeed, when the SDS concentration increased, the size of the initial micelles in the emulsion system increased, resulting in formation of larger PS particles.<sup>23</sup> In all cases, PS nanoparticles with narrow size distribution were obtained (Fig. S1†). These PS nanoparticles were stored in water as stable stock solutions until they were used for the fabrication of the PS nanoparticles template.

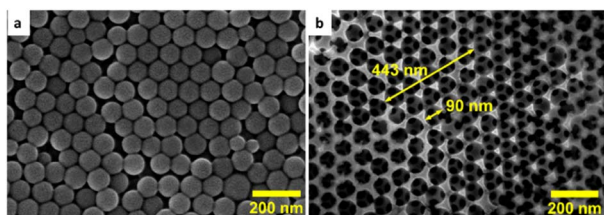


Fig. 2 SEM images collected on the surface of (a) a PS (90 nm)-FTO template and (b) a 3D-MoS<sub>x</sub>-FTO films after removing the PS particles.

Subsequently, an aliquot volume of a stock solution of PS nanoparticles was drop-casted on a fluorine-doped tin oxide (FTO) substrate surface to obtain a PS-FTO template after the natural evaporation of the solvent in air. The PS-FTO substrate was then immersed in an electrolyte solution constituted of 1 mM (NH<sub>4</sub>)<sub>2</sub>[Mo<sub>3</sub>S<sub>13</sub>] in 0.1 M LiClO<sub>4</sub> and held at a constant potential of 0.4 V vs. NHE. At this potential, [Mo<sub>3</sub>S<sub>13</sub>]<sup>2-</sup> followed a two-electron oxidation process generating amorphous coordination polymer MoS<sub>x</sub><sup>19</sup> which filled in the space between the PS spherical particles. Immersing the resultant MoS<sub>x</sub>-PS-FTO film into dichloromethane solvent induced the dissolution of

PS nanoparticles generating the final 3D-MoS<sub>x</sub>-FTO film (Fig. 2). We hypothesize that the quality of the 3D-MoS<sub>x</sub>-FTO film will depend on (i) the thickness of the PS template, (ii) the size of the PS nanoparticles, and (iii) the amount of MoS<sub>x</sub> deposited.

Theoretical calculation revealed that the 3D-MoS<sub>x</sub> samples possessed significantly superior specific surface areas to that of the bulk MoS<sub>x</sub> film (Table S2†). When comparing PS templates with the same thickness, the one made of smaller PS nanoparticles will provide 3D-MoS<sub>x</sub> with higher specific surface area.

Hence, we first examined the eventual impact of the size of the PS nanoparticles on the quality of the obtained MoS<sub>x</sub> film. The PS nanoparticles having average diameter of 35, 50, 60, 70 and 90 nm were chosen for examination. To this end, the PS particles were re-dispersed into water to obtain a stable colloidal solution having PS weight concentration of 4 mg mL<sup>-1</sup>. An aliquot volume of this colloidal solution was drop-casted onto the surface of a FTO electrode. The solvent was dried naturally to obtain PS-FTO template (Fig. 2a). The PS mass loading was kept at 400 μg cm<sup>-2</sup> generating an average film thickness of 1650 nm for 90 nm PS particles (Fig. S2†). Fig. S3† shows the surface morphologies of these PS-FTO films. The film with 35 nm PS particles appeared compact with low

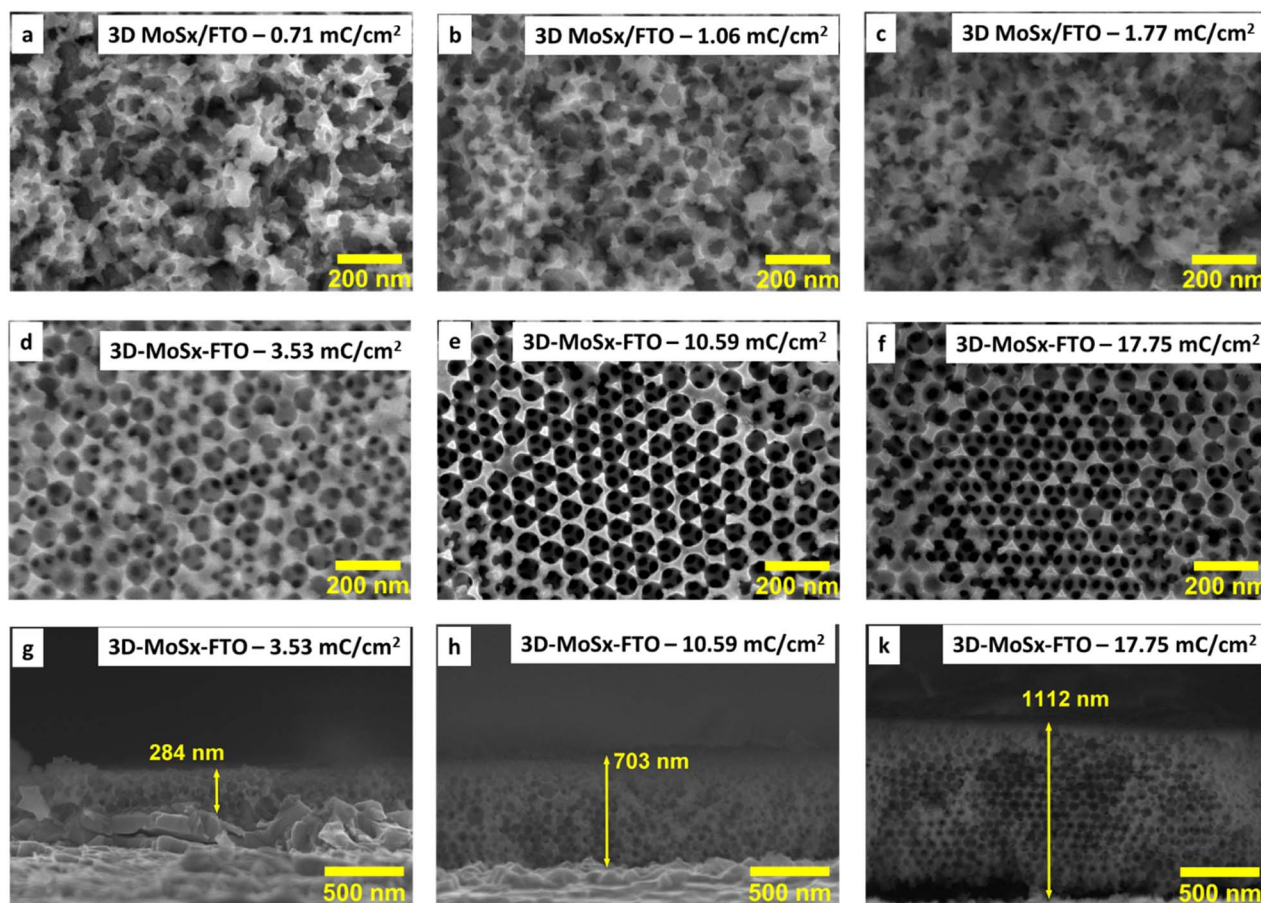


Fig. 3 (a)–(f) SEM images collected on the surface of 3D-MoS<sub>x</sub> films grown on FTO substrate using the PS-90 nm template but with different deposition charge densities; (g)–(k) SEM cross-section observed for the 3D-MoS<sub>x</sub> films grown with the deposition charge densities of 3.53, 10.59 and 17.65 mC cm<sup>-2</sup>.



spacing between the particles. Increasing the particle size generates larger space between the particles. The 3D-MoS<sub>x</sub> film after the removal of 90 nm PS particles shows highly ordered arrangement of MoS<sub>x</sub> in a honeycomb-like structure (Fig. 2b). The spherical space left between the MoS<sub>x</sub> frame was determined to be *ca.* 90 nm in diameter which was exactly the size of the PS nanoparticles used.

We then optimized the growth of MoS<sub>x</sub> on the PS (90 nm)-FTO template by varying the amount of deposition charge. The same oxidation potential of 0.4 V *vs.* RHE and the same deposition bath made of 1 mM (NH<sub>4</sub>)<sub>2</sub>[MoS<sub>4</sub>] in 0.1 M LiClO<sub>4</sub> electrolyte solution were employed. When the deposition was

over, the resultant dark brown films were collected and intensively washed with DI water to remove unwanted species such as LiClO<sub>4</sub> or (NH<sub>4</sub>)<sub>2</sub>[MoS<sub>4</sub>] that could adsorb on the MoS<sub>x</sub>/PS film. The PS particles were finally removed by repeating the immersion of MoS<sub>x</sub>-PS-FTO films in dichloromethane to produce the 3D-MoS<sub>x</sub> films on FTO substrate (see ESI† for details). Fig. 3a–f show the surface morphology of the 3D-MoS<sub>x</sub> films after removing the PS nanoparticles template. Using a low deposition charge of 0.71–1.77 mC cm<sup>−2</sup> resulted in the formation of irregular MoS<sub>x</sub> films where the ordered structure of PS bread templates was not retained (Fig. 3a–c). It is likely because the low deposition charge induced the growth of thin-wall MoS<sub>x</sub> in the space between the PS nanoparticles which were subsequently collapsed when the PS nanoparticle template was dissolved. When the deposition charge of 3.53 mC cm<sup>−2</sup> was used, more robust MoS<sub>x</sub> wall was deposited which help keep the ordered, honeycomb-like structure of the film intact after the dissolution of the PS nanoparticles (Fig. 3d–f). The cross-section analysis shows clearly the regular three-dimension (3D) structure with a film thickness of 284 nm (Fig. 3g). Indeed, this thickness is equivalent to three layers of PS particles as each particle has an average diameter of 90 nm. This film grew from the FTO surface, indicating a good penetration of [Mo<sub>3</sub>S<sub>13</sub>]<sup>2−</sup> precursor into the porous PS template. It is also interesting to note that the whole PS particles were successfully removed, including the first layer lying on the FTO surface. In fact, the complete removal of the electrical isolating PS template is critical to ensure good

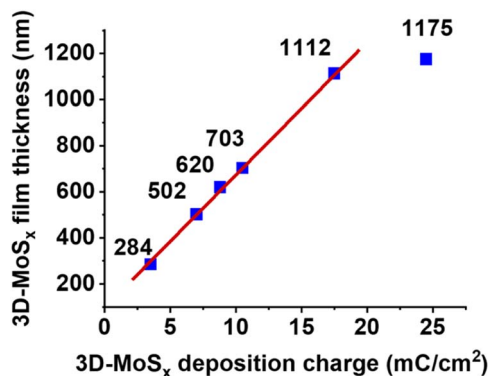


Fig. 4 The evolution of 3D-MoS<sub>x</sub> film thickness in function of the deposition charge density consumed.

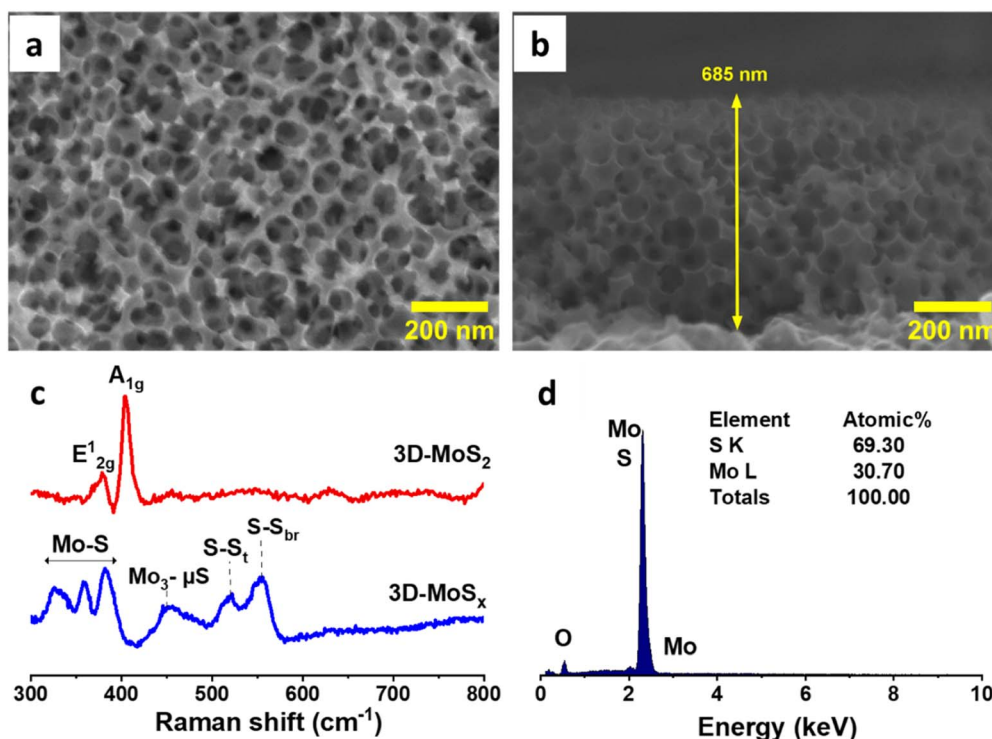


Fig. 5 (a) Surface and (b) cross-section SEM images collected on the 3D-MoS<sub>2</sub> film which was generated from annealing the 3D-MoS<sub>x</sub> film (made with a deposition charge of 10.59 mC cm<sup>−2</sup>); (c) Raman spectra collected on 3D-MoS<sub>2</sub> and 3D-MoS<sub>x</sub> samples employing a 532 nm laser excitation, (d) EDX analysis conducted on the 3D-MoS<sub>2</sub> film.



conductivity and thus good electrochemical catalytic activity of the  $\text{MoS}_x$  frame.

We then applied the same deposition charge density of  $3.53 \text{ mC cm}^{-2}$  for other PS-FTO templates. After removing the PS template, the resultant  $\text{MoS}_x$  films showed porous but disordered structure if small PS particle size of 35–60 nm was used for the template construction (Fig. S4a–c†). The template with PS particle size of 70 nm resulted in  $\text{MoS}_x$  film with a rather ordered structure wherein  $\text{MoS}_x$  wall was broken (collapsed) in some location, likely due to its thin and fragile characteristics (Fig. S4d†). Thus, we decided to choose the PS particles of 90 nm in diameter for the construction of PS-FTO template for further optimization of the 3D- $\text{MoS}_x$  fabrication.

While holding the same PS-90 nm/FTO template electrode in the deposition bath at the same oxidative deposition potential of 0.4 V vs. RHE, we extended the deposition time in order to increase the amount of  $\text{MoS}_x$  deposited and thus increase the thickness of the resultant 3D- $\text{MoS}_x$  film. Fig. 3g–k show the cross-section observation of resultant 3D- $\text{MoS}_x$  films having different thickness. Fig. 4 shows the evolution of  $\text{MoS}_x$  film thickness in function of the deposition charge consumed. A linear dependence was found for the deposition charge in the range of  $3.53$ – $17.85 \text{ mC cm}^{-2}$ , corresponding to the film thickness range of 284–1112 nm. SEM analysis conducted on the surface of the resultant 3D- $\text{MoS}_x$  films shows regular honeycomb-like pattern (Fig. 3e, f and S5a†). We could obtain even thicker films having thickness of 1175 nm by consuming a deposition charge density of  $24.71 \text{ mC cm}^{-2}$ . However, this film shows irregular surface morphology where both honeycomb-like pattern and compact  $\text{MoS}_x$  domains are found (Fig. S5b†). The thickness of 1112 nm corresponds to 12 layers of PS beads of 90 nm diameter. It means that (i) the  $[\text{Mo}_3\text{S}_{13}]^{2-}$  precursor can deeply penetrate into the  $\mu\text{m}$ -thick PS films, and (ii) the resultant  $\mu\text{m}$ -thick 3D- $\text{MoS}_x$  is robust and remain intact during the dissolution of PS beads.

### Fabrication of 3D- $\text{MoS}_2$

The aforementioned 3D- $\text{MoS}_x$  films were then annealed at  $450^\circ\text{C}$  in an inert atmosphere of Ar flux for 3 hours. Under this thermal treatment, the amorphous  $\text{MoS}_x$  transformed into

crystalline  $\text{MoS}_2$  releasing sulfur vapor ( $\text{MoS}_{x(s)} \rightarrow \text{MoS}_{2(s)} + \text{S}_{8(g)}$ ).<sup>21</sup> Raman analysis clearly evidenced the formation of  $\text{MoS}_2$  with two characteristic vibration bands at 380 and  $403 \text{ cm}^{-1}$  being assignable to the  $\text{E}_{1g}$  and  $\text{A}_{2g}$  vibrational modes of  $\text{MoS}_2$  crystalline structure (Fig. 5c).<sup>5d</sup> SEM analysis conducted on the resultant 3D- $\text{MoS}_2$  film revealed that it conserved the initial structure of the 3D- $\text{MoS}_x$  film. Indeed, the surface of 3D- $\text{MoS}_2$  film shows the regular honeycomb-like patterns with the spacing volume of ca. 90 nm together with the appearance of some damages, probably due to the rapid evaporation of sulfur by-product that weakens the  $\text{MoS}_2$  wall (Fig. 5a). SEM cross-section analysis revealed the similar thickness of the resultant 3D- $\text{MoS}_2$  (Fig. 5b) and the initial amorphous 3D- $\text{MoS}_x$  film (Fig. 4h). The EDX analysis showed a Mo : S atomic ratio of 1 : 2.3 (Fig. 5d) that was lower in comparison to that of the as-prepared  $\text{MoS}_x$  film, namely Mo : S atomic ratio of 1 : 3 (Fig. S6†).

### Assaying catalytic $\text{H}_2$ evolution

We then assayed the  $\text{H}_2$  evolving catalytic activity of 3D- $\text{MoS}_x$  and 3D- $\text{MoS}_2$  films in a strong acidic electrolyte solution, namely the 0.5 M  $\text{H}_2\text{SO}_4$  (pH 0.3) solution. Prior to measurements, the electrolyte solution was purged with a  $\text{N}_2$  flux to eliminate the dissolved  $\text{O}_2$ . In order to examine the potential advantages of the 3D-structuring approach, bulk  $\text{MoS}_x$  thin films grown on FTO electrodes without employing the PS template were fabricated and used as reference samples. The deposition charge density was maintained identically to that deployed for making 3D- $\text{MoS}_x$  films to ensure an identical amount of bulk  $\text{MoS}_x$  and 3D- $\text{MoS}_x$  grown. Fig. 6a shows  $I$ - $V$  curves recorded on a 3D- $\text{MoS}_x$  electrode and a bulk  $\text{MoS}_x$  counterpart, both obtained by employing a deposition charge density of  $3.53 \text{ mC cm}^{-2}$ . Obviously, at any potential the 3D- $\text{MoS}_x$  electrode (red trace) shows higher catalytic current density than that obtained for the bulk  $\text{MoS}_x$  electrode (blue trace). To sustain the benchmarking catalytic current density of  $10 \text{ mA cm}^{-2}$ , the 3D- $\text{MoS}_x$ - $3.53 \text{ mC}$  catalyst electrode requires 50 mV less than the bulk- $\text{MoS}_x$ - $3.53 \text{ mC}$  counterpart. The catalytic current density obtained at  $-0.3 \text{ V vs. RHE}$  are 15.6 and  $9.5 \text{ mA cm}^{-2}$  for the 3D- $\text{MoS}_x$ - $3.53 \text{ mC}$  and bulk- $\text{MoS}_x$ - $3.53 \text{ mC}$  electrodes, respectively. Tafel plots in the low kinetic region show

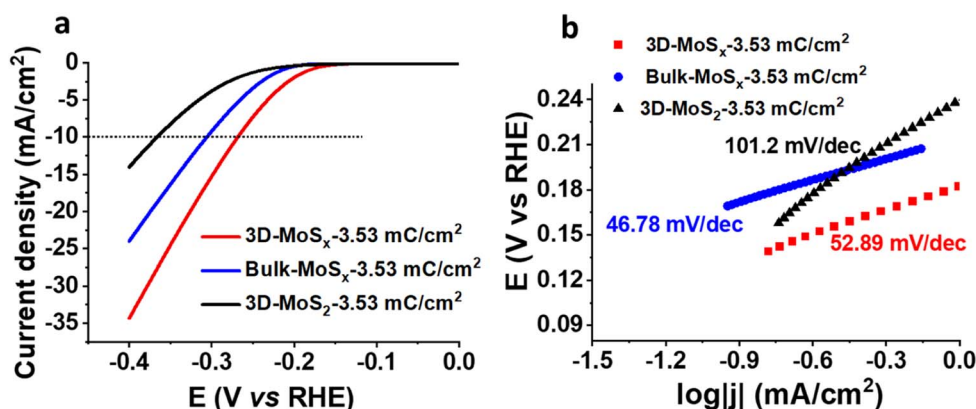


Fig. 6 (a)  $I$ - $V$  curves and (b) corresponding Tafel plots recorded for the bulk- $\text{MoS}_x$ - $3.53 \text{ mC cm}^{-2}$ , 3D- $\text{MoS}_x$ - $3.53 \text{ mC cm}^{-2}$ , and the 3D- $\text{MoS}_2$ - $3.53 \text{ mC cm}^{-2}$  catalyst electrodes. Electrolyte was a 0.5 M  $\text{H}_2\text{SO}_4$  (pH 0.3) solution. Potential scan rate was  $5 \text{ mV s}^{-1}$ .



comparable slopes, namely 53 mV per decade for the 3D-MoS<sub>x</sub>-3.53 mC catalyst electrode and 47 mV per decade for the bulk-MoS<sub>x</sub>-3.53 mC catalyst electrode (Fig. 6b). It suggests the similar H<sub>2</sub> evolution mechanism occurring on these two catalyst electrodes which is expected as these two electrodes are identical in the chemical nature but only different in topology.

Even when displaying the same regular inverse opal structure to that of the amorphous 3D-MoS<sub>x</sub>-3.53 mC cm<sup>-2</sup> electrode, the crystalline 3D-MoS<sub>2</sub>-3.53 mC cm<sup>-2</sup> electrode showed significantly lower catalytic activity (black trace, Fig. 6a). At -0.3 V vs. RHE, the catalytic current densities were 3.85 mA cm<sup>-2</sup> and 15.6 mA cm<sup>-2</sup> for the 3D-MoS<sub>2</sub>-3.53 mC cm<sup>-2</sup> and the 3D-MoS<sub>x</sub>-3.53 mC cm<sup>-2</sup> electrodes, respectively. We note that the 3D-MoS<sub>2</sub>-3.53 mC cm<sup>-2</sup> electrode was even less active than the bulk-MoS<sub>x</sub>-3.53 mC cm<sup>-2</sup> counterpart (Fig. 6a). It clearly demonstrates that the MoS<sub>x</sub>-to-MoS<sub>2</sub> crystallization causes a significant loss of catalytic ability. The Tafel slope value of 101.2 was deduced for the crystalline 3D-MoS<sub>2</sub>-3.53 mC cm<sup>-2</sup> which is significantly higher than those obtained for the MoS<sub>x</sub> electrodes (Fig. 6b). This result indicates different HER mechanisms occurring on the MoS<sub>x</sub> and MoS<sub>2</sub> catalysts. While the Heyrovski and Tafel steps dominate the H<sub>2</sub> evolution on MoS<sub>x</sub>

catalyst, the Volmer step dominates the reaction on 3D-MoS<sub>2</sub>-3.53 mC cm<sup>-2</sup> counterpart.<sup>24</sup>

We then assayed the stability of 3D-MoS<sub>x</sub>-3.53 mC cm<sup>-2</sup> and 3D-MoS<sub>2</sub>-3.53 mC cm<sup>-2</sup> catalysts under the catalytic H<sub>2</sub> evolution conditions in a 0.5 M H<sub>2</sub>SO<sub>4</sub> electrolyte solution. To this end, the chronopotentiometry analysis was conducted at the benchmarking catalytic current density of 10 mA cm<sup>-2</sup> for 6 hours. It was found that the 3D-MoS<sub>x</sub>-3.53 mC cm<sup>-2</sup> catalyst required a smaller cathodic potential in comparison to the 3D-MoS<sub>2</sub>-3.53 mC cm<sup>-2</sup> counterpart to sustain the same catalytic current density (Fig. S7a†). It is consistent with the fact that the 3D-MoS<sub>x</sub>-3.53 mC cm<sup>-2</sup> is more catalytically active than the 3D-MoS<sub>2</sub>-3.53 mC cm<sup>-2</sup>. Interestingly, during the first 10 minutes of operation, potential which was required to apply on the 3D-MoS<sub>x</sub>-3.53 mC cm<sup>-2</sup> catalyst decreased from -0.34 V vs. RHE to a steady value of -0.31 V vs. RHE (Fig. S8†). It clearly demonstrated an activation stage of amorphous MoS<sub>x</sub> catalyst prior to operation.<sup>6c</sup> When extending the catalytic operation time, higher cathodic potential is required for the 3D-MoS<sub>x</sub>-3.53 mC cm<sup>-2</sup> catalyst suggesting possible degradation (Fig. 7b, red trace). The same tendency was observed for the 3D-MoS<sub>2</sub>-3.53 mC cm<sup>-2</sup> counterpart in the first 3 hours of operation (Fig. S7b,† black trace). After that, potential suddenly jumped to

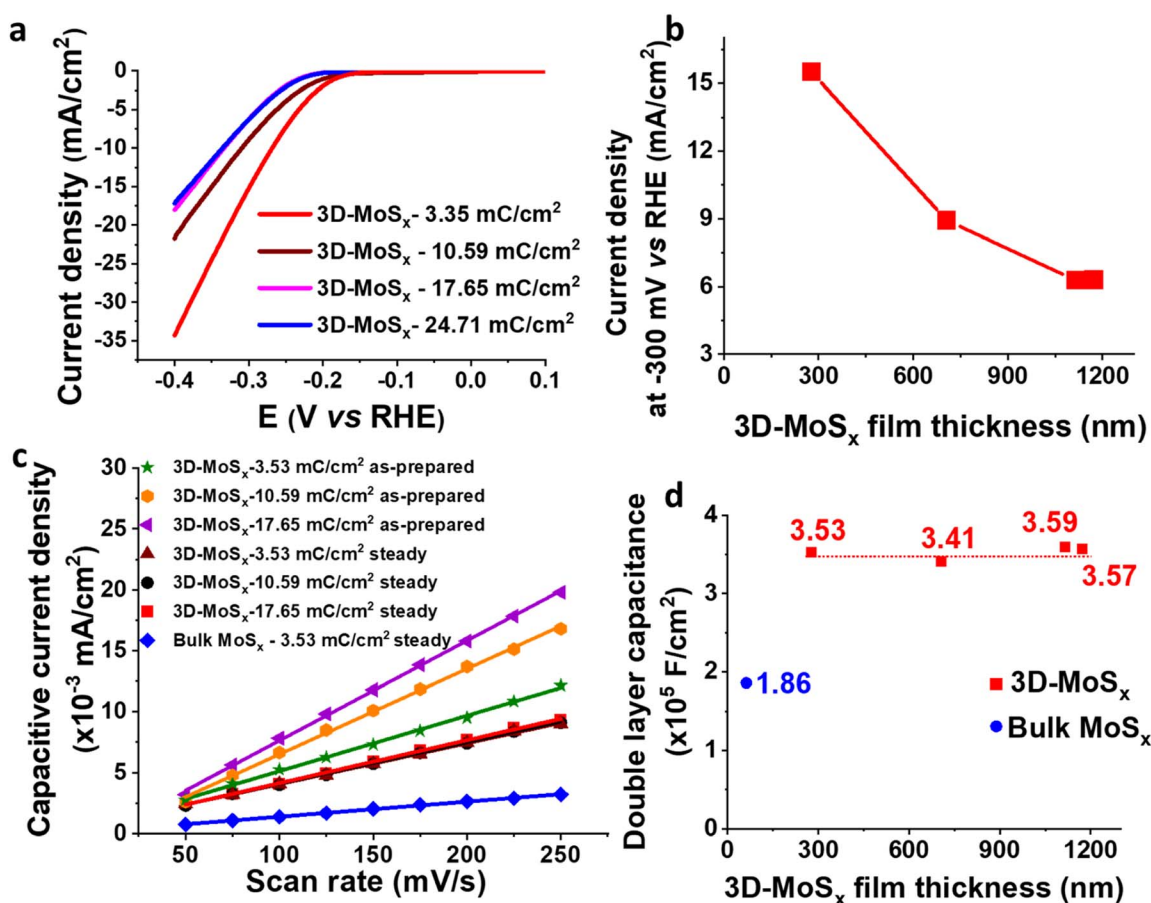


Fig. 7 3D-MoS<sub>x</sub> films obtained by using different deposition charge densities, thus having different thickness. (a) *I*-*V* curves, (b) evolution of catalytic current density obtained at -0.3 V vs. RHE in function of the 3D-MoS<sub>x</sub> film thickness, (c) capacitive current density recorded at 0.1 V vs. RHE in function of potential scan rate for the as-prepared 3D-MoS<sub>x</sub> electrodes and for these electrodes after reaching the steady performance, and (d) evolution of double layer capacitance in function of the 3D-MoS<sub>x</sub> film thickness (catalyst films already reach its steady performance).

*ca.*  $-0.6$  V *vs.* RHE (and then more cathodic potential). At this moment, we observed a detachment of 3D-MoS<sub>2</sub> from the FTO electrode surface. This catalyst detachment could explain for the complete degradation of the catalytic performance.

In order to avoid the catalyst detachment, we conducted the H<sub>2</sub> evolution assay in a milder condition, namely a chronoamperometry analysis at the constant cathodic potential of  $-0.3$  V *vs.* RHE. The 3D-MoS<sub>2</sub>-3.53 mC cm<sup>-2</sup> showed a slight superior stability during the operation in comparison to the 3D-MoS<sub>x</sub>-3.53 mC cm<sup>-2</sup>. As a demonstration, after 6 h of operation, the 3D-MoS<sub>x</sub>-3.53 mC cm<sup>-2</sup> catalyst electrode lost 73% of its initial catalytic current density (Fig. S7b,† red trace) while the loss was 55% for the 3D-MoS<sub>2</sub>-3.53 mC cm<sup>-2</sup> one (Fig. S7b,† black trace).

SEM analysis performed on these catalyst electrodes after 6 h-catalysis revealed that the regular inverse opal structure of the 3D-MoS<sub>2</sub>-3.53 mC cm<sup>-2</sup> catalyst remained whereas the initial structure of 3D-MoS<sub>x</sub>-3.53 mC cm<sup>-2</sup> has been partially corrupted (Fig. S9†).

We then focused on examining the catalytic activities of the 3D-MoS<sub>x</sub> electrodes having different thickness that had been grown by applying different deposition charge density. Fig. 7a shows the *I*-*V* curves recorded on these electrodes. Fig. 7b plots the catalytic current density obtained at potential of  $-0.3$  V *vs.* RHE in function of the film thickness. It can be seen that the 3D-MoS<sub>x</sub>-3.53 mC cm<sup>-2</sup> with the thickness of 284 nm shows the highest catalytic current density. Thicker film shows lower catalytic activity. It demonstrates that the 3D-structuring strategy has its limitation. It could help improving the catalytic activity in comparison to the bulk catalyst film but the effect reaches a plateau after a certain value of film thickness.

### Investigation on the reason behind the limitation of catalytic activity

It is regrettable that micron-meter-thickness 3D-MoS<sub>x</sub> films which possess high density of MoS<sub>x</sub> catalyst could not offer superior catalytic activities as we expected. To understand the reason behind the limitation of catalytic activity, we first measured the surface wettability of the bulk-MoS<sub>x</sub>, 3D-MoS<sub>x</sub> and 3D-MoS<sub>2</sub> films. Water contact angles of 113°, 127° and 128° were determined for the bulk-MoS<sub>x</sub>-3.53 mC cm<sup>-2</sup>, 3D-MoS<sub>x</sub>-3.53 mC cm<sup>-2</sup> and 3D-MoS<sub>2</sub>-3.53 mC cm<sup>-2</sup> films, respectively (Fig. S10†). It means the creation of the inverse opal structure with empty volume where the air could be trapped, *e.g.* sphere diameter of *ca.* 90 nm, insignificantly alters the hydrophobicity of the MoS<sub>x</sub> and MoS<sub>2</sub> surface. This result indicates that the superiority in catalytic ability of 3D-MoS<sub>x</sub> could be the result of its higher specific electrochemical surface area (ECSA) and/or higher amount of MoS<sub>x</sub> catalyst exposed to the electrolyte but not due to its surface wettability. We determined the relative ECSA of these samples by measuring their double layer capacitance. Fig. S11† shows the *I*-*V* curves recorded on these catalyst electrodes immersed in the same 0.5 M H<sub>2</sub>SO<sub>4</sub> electrolyte solution in the capacitive potential region, namely 0.05 to 0.15 V *vs.* RHE, at different potential scan rates. Plotting the capacitive current obtained at 0.1 V *vs.* RHE in function of the potential

scan rate gives the slope which represents the capacitance (Fig. 7c). The as-prepared 3D-MoS<sub>x</sub>-3.53 mC cm<sup>-2</sup> electrode displayed a double layer capacitance (*C*<sub>dl</sub>) of  $4.56 \times 10^{-5}$  F cm<sup>-2</sup>. Increasing the deposition charge, thus increasing the thickness of the 3D-MoS<sub>x</sub> films led to an increment of the double layer capacitance, thus an increment of the ECSA. The capacitance of  $7.01 \times 10^{-5}$  F cm<sup>-2</sup> and  $8.19 \times 10^{-5}$  F cm<sup>-2</sup> were calculated for the 3D-MoS<sub>x</sub>-10.59 mC cm<sup>-2</sup> and the 3D-MoS<sub>x</sub>-17.65 mC cm<sup>-2</sup>, respectively (Fig. 7c). Using 1 mM ferrocene (Fc) in dichloromethane as the redox probe (Fig. S12a†), we found that the cathodic current density of the Fc<sup>+</sup>/Fc redox couple increased linearly with the 3D-MoS<sub>x</sub> film's deposition charge (Fig. S12b†) and its thickness (Fig. S12c†). These results clearly demonstrated that increasing the deposition charge resulted in an increment of the electrochemical surface area of 3D-MoS<sub>x</sub> films.

When the 3D-MoS<sub>x</sub>-3.53 mC cm<sup>-2</sup> catalyst electrode already reached its steady catalytic performance for the H<sub>2</sub> evolution, it displayed a *C*<sub>dl</sub> of  $3.53 \times 10^{-5}$  F cm<sup>-2</sup> which was slightly smaller than the value of  $4.56 \times 10^{-5}$  F cm<sup>-2</sup> determined for the same electrode before used for catalysis. Under similar conditions, the bulk-MoS<sub>x</sub>-3.53 mC cm<sup>-2</sup> catalyst electrode displayed a *C*<sub>dl</sub> of  $1.86 \times 10^{-5}$  F cm<sup>-2</sup>. It means the 3D-MoS<sub>x</sub>-3.53 mC cm<sup>-2</sup> catalyst has two times higher electrochemical surface area than the bulk-MoS<sub>x</sub>-3.53 mC cm<sup>-2</sup> catalyst (Fig. 7c). Hence, we can attribute the superior catalytic activity of the 3D-MoS<sub>x</sub> catalyst to its superior active surface area in comparison to the bulk-MoS<sub>x</sub>-3.53 mC cm<sup>-2</sup> counterpart. Looking at the 3D-MoS<sub>x</sub>-3.53 mC cm<sup>-2</sup> and the 3D-MoS<sub>2</sub>-3.53 mC cm<sup>-2</sup>, these catalyst electrodes displayed similar capacitance, thus similar specific electrochemical surface area (Fig. S13†).

Interestingly, we found that when the 3D-MoS<sub>x</sub> catalysts reached its steady catalytic performance, it displayed similar capacitance regardless of its thickness, thus similar electrochemical surface areas (Fig. 7c and d). This result suggests that for the thick 3D-MoS<sub>x</sub> films, only a few layers count from the MoS<sub>x</sub>/electrolyte interface (thus count from the MoS<sub>x</sub> top surface) are effective for the H<sub>2</sub> evolution catalysis but not the whole film volume. As mentioned above, the 284 nm-thick 3D-MoS<sub>x</sub>-3.53 mC cm<sup>-2</sup> catalyst film showed the highest catalytic current density. We note that 284 nm is equal to 3-layers of PS nanoparticles, thus 3-layers of MoS<sub>x</sub>. Thus, it is likely that only the 3-top-layers of MoS<sub>x</sub> films is catalytically effective for the H<sub>2</sub> evolution.

To better understand this phenomenon, we investigated the penetration of aqueous H<sub>2</sub>SO<sub>4</sub> electrolyte in the 3D-MoS<sub>x</sub> electrode volume. To this end, a 707 nm-thick 3D-MoS<sub>x</sub>-10.59 mC cm<sup>-2</sup> electrode was immersed in an electrolyte constituted of 1 mM CuSO<sub>4</sub> and 0.5 M H<sub>2</sub>SO<sub>4</sub>. A cyclic voltammetry polarization in the potential range of  $-0.7$  to  $0.2$  V *vs.* Ag/AgCl was then applied to the electrode with a potential scan rate of 50 mV s<sup>-1</sup> (Fig. S14†). It resulted in the deposition of Cu on the 3D-MoS<sub>x</sub>-10.59 mC cm<sup>-2</sup> electrode. When the deposition was over, the electrode was taken out and then immersed in DI water. The EDS elemental mapping conducted on the cross-section of this electrode showed the homogeneous distribution of Cu, Mo and S elements (Fig. S15†). It clearly demonstrated that the aqueous



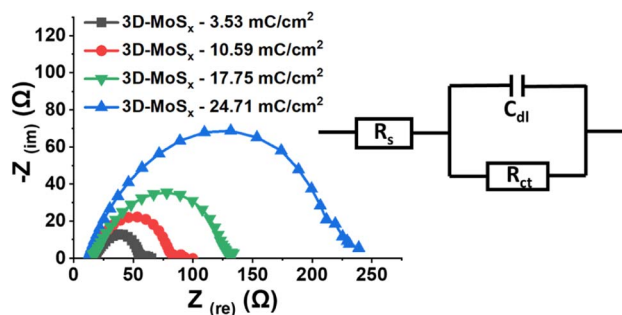


Fig. 8 Nyquist plots obtained on 3D-MoS<sub>x</sub> electrodes immersed in a pH 0.3 H<sub>2</sub>SO<sub>4</sub> electrolyte at  $-0.4$  V vs. RHE and equivalent electrical circuit used for fitting the experimental data.

electrolyte deeply penetrated through all the thickness of the 3D-MoS<sub>x</sub> films.

Hence, prior to the H<sub>2</sub> evolution catalysis, the electrolyte could penetrate into the whole volume of the 3D-MoS<sub>x</sub> catalyst. However, when the H<sub>2</sub> evolution occurs during cathodic polarizations, the generated H<sub>2</sub> bubbles can adsorb on the MoS<sub>x</sub> layers thanks to the H<sub>2</sub> storage capacity by adsorption of MoS<sub>x</sub>.<sup>25</sup> Thus, the layers being close to the FTO substrate surface are then no longer effective for the H<sub>2</sub> generation. In other words, only the 3-top-layers of MoS<sub>x</sub> films, where the H<sub>2</sub> bubbles generated can be evacuated, will be effective for the H<sub>2</sub> generation.

Electrochemical impedance spectroscopic (EIS) analysis is a powerful method to track the electron transfer happening during the H<sub>2</sub> evolution catalysis. Thus, we conducted the EIS analysis on 3D-MoS<sub>x</sub> electrodes at a constant potential of  $-0.3$  V vs. RHE where the catalytic H<sub>2</sub> evolution occurred (see ESI† for more details). Fig. 8 shows the obtained Nyquist plots and the simple Randles equivalent electric circuit that we employed to fit the experimental data.  $R_s$  is the external series resistance,  $R_{ct}$  is the charge transfer resistance at the electrode/electrolyte interface and  $C_{dl}$  is the capacitance of the 3D-MoS<sub>x</sub> samples. Results obtained from the fitting are presented in Table 1. It can be seen that  $R_{ct}$  increases drastically with increment of the MoS<sub>x</sub> film thickness. It means a thicker 3D-MoS<sub>x</sub> film has a higher resistance to the electron transfer. In addition, the EIS analyses showed similar capacitance  $C_{dl}$  values that are in agreement to the similar ECSA values of the 3D-MoS<sub>x</sub> electrodes. The results re-confirmed the limited

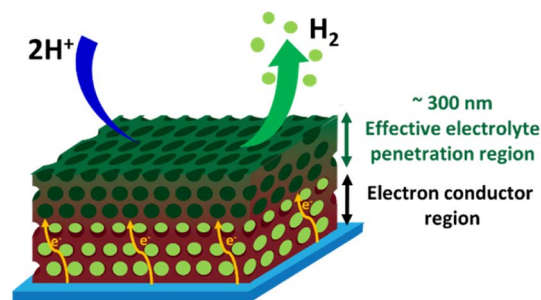


Fig. 9 Schematic illustration on the operation of an inverse opal MoS<sub>x</sub> catalyst.

interfacial area between 3D-MoS<sub>x</sub> electrodes and the electrolyte.

Fig. 9 illustrates schematically the operation of a 3D-MoS<sub>x</sub> or a 3D-MoS<sub>2</sub> catalyst electrode. The electrolyte could penetrate effectively into the whole volume of the porous catalyst films. When the H<sub>2</sub> evolution occurs, the H<sub>2</sub> bubbles generated within the depleted layers of 3D-MoS<sub>x</sub> (or 3D-MoS<sub>2</sub>), e.g. the layers stand closely to the FTO substrate surface, could not be effectively evacuated. Thus, the depleted layers of 3D-MoS<sub>x</sub> (or 3D-MoS<sub>2</sub>) will no longer be active for the H<sub>2</sub> evolution. Therefore, only the few-top-layers of the 3D-MoS<sub>x</sub> (or 3D-MoS<sub>2</sub>) films where H<sub>2</sub> bubbles can be effectively evacuated will be effective for the H<sub>2</sub> evolution catalysis. The effective thickness for the H<sub>2</sub> evolution catalysis in water is about 300 nm, being equivalent to 3-top-layers of 3D-MoS<sub>x</sub> and 3D-MoS<sub>2</sub>. Given that the MoS<sub>x</sub> and MoS<sub>2</sub> have low electrical conductivities of  $10^{-4}$  to  $10^{-6}$  S cm<sup>-1</sup>,<sup>26</sup> thicker film displays higher resistance. Consequently, thicker 3D-MoS<sub>x</sub> film shows lower H<sub>2</sub> evolution catalytic activity. Even having the same effective thickness, and thus the same electrochemical surface area, the 3D-MoS<sub>x</sub> is significantly more active than the 3D-MoS<sub>2</sub> counterpart. The following reasons could be evoked to explain this phenomenon: (i) the intrinsic activity of an active center within the MoS<sub>2</sub> is significantly lower than that of an active center within the MoS<sub>x</sub>, and/or (ii) the actual number of active sites within MoS<sub>2</sub> is significantly lower than that within MoS<sub>x</sub> as only the edges of MoS<sub>2</sub> is active but not its basal plane.<sup>14,27</sup>

## Conclusion

We have successfully fabricated amorphous MoS<sub>x</sub> catalyst electrodes having regular inverse opal structure by using small polystyrene nanoparticles as hard templates. By this fabrication process, we were able to tune the empty space between the MoS<sub>x</sub> wall, thus the density of MoS<sub>x</sub> deposited, by varying the polystyrene particle size. However, using small particles of 30–70 nm diameter size tends to result in 3D-MoS<sub>x</sub> films where the MoS<sub>x</sub> wall is thin and fragile which can be collapsed in some location. Using the template made of 90 nm diameter size polystyrene nanoparticles produces the robust 3D-MoS<sub>x</sub> structure whose thickness can be easily tuned, e.g. up to micrometer scale, by extending the MoS<sub>x</sub> electrodeposition time. Annealing the 3D-MoS<sub>x</sub> films at 450 °C under Ar inert atmosphere resulted

Table 1 EIS parameters calculated from simple Randles equivalent circuit

Sample	$R_s$ (ohm)	$R_{ct}$ (ohm)	$C_{dl}$ (F)
3D-MoS <sub>x</sub> -3.53 mC cm <sup>-2</sup>	19.65	36.45	$11.61 \times 10^{-5}$
3D-MoS <sub>x</sub> -10.59 mC cm <sup>-2</sup>	17.64	64.86	$11.31 \times 10^{-5}$
3D-MoS <sub>x</sub> -17.65 mC cm <sup>-2</sup>	18.55	112.3	$9.96 \times 10^{-5}$
3D-MoS <sub>x</sub> -24.71 mC cm <sup>-2</sup>	12.67	216.4	$10.49 \times 10^{-5}$



in the formation of crystalline 3D-MoS<sub>2</sub> wherein the regular inverse opal structure of the initial MoS<sub>x</sub> film was retained. During catalytic operation, regardless of their actual thickness, the 3D-MoS<sub>x</sub> and 3D-MoS<sub>2</sub> films display the same effective thickness which is estimated to be *ca.* 284 nm where the water molecule could penetrate and the H<sub>2</sub> bubbles can be effectively evacuated. Having films thicker than 284 nm is not beneficial and disfavours the H<sub>2</sub> evolution catalysis as the inner MoS<sub>2</sub> and MoS<sub>x</sub> layers increase the film resistance. The 3D-MoS<sub>x</sub>-284 nm catalyst film shows the highest catalytic activity which is significantly higher than those obtained using the 3D-MoS<sub>2</sub>-284 nm counterpart as well as the bulk-MoS<sub>x</sub> reference film. These results demonstrate that engineering a regular inverse opal structure is a good strategy to enhance the H<sub>2</sub> evolution catalytic activity of amorphous MoS<sub>x</sub> catalyst, but a fine optimization should be performed to obtain an appropriate thickness, *e.g.* being close to the effective thickness for the penetration of electrolyte.

## Author contributions

Thai D. Nguyen: investigation, writing – original draft; Huong T. L. Phung: investigation; Duc N. Nguyen: methodology, formal analysis; Anh D. Nguyen: conceptualization, methodology, writing-editing/review, project administration, funding acquisition, supervision; Phong D. Tran: conceptualization, writing-editing/review, supervision.

## Conflicts of interest

The authors declare no conflict of interest.

## Acknowledgements

This research was funded by University of Science and Technology of Hanoi under the grant number USTH.FAS.01/21-22.

## References

- (a) N. S. Lewis and D. G. Nocera, *Proc. Natl. Acad. Sci. U. S. A.*, 2006, **103**, 15729–15735; (b) D. G. Nocera, *Inorg. Chem.*, 2009, **48**, 10001–10017.
- N. Dubouis and A. Grimaud, *Chem. Sci.*, 2019, **10**, 9165–9181.
- D. Strmcnik, P. P. Lopes, B. Genorio, V. R. Stamenkovic and N. M. Markovic, *Nano Energy*, 2016, **29**, 29–36.
- (a) J. N. Hansen, H. Prats, K. K. Toudahl, N. Mørch Secher, K. Chan, J. Kibsgaard and I. Chorkendorff, *ACS Energy Lett.*, 2021, **6**, 1175–1180; (b) T. F. Jaramillo, K. P. Jørgensen, J. Bonde, J. H. Nielsen, S. Hørch and I. Chorkendorff, *Science*, 2007, **317**, 100–102.
- (a) S. Parvin, A. Kumar, A. Ghosh and S. Bhattacharyya, *Chem. Sci.*, 2020, **11**, 3893–3902; (b) J. Kibsgaard and T. F. Jaramillo, *Angew. Chem., Int. Ed.*, 2014, **53**, 14433–14437; (c) D. Merki, S. Fierro, H. Vrubel and X. Hu, *Chem. Sci.*, 2011, **2**, 1262–1267; (d) P. D. Tran, T. V. Tran, M. Orio, S. Torelli, Q. D. Truong, K. Nayuki, Y. Sasaki, S. Y. Chiam, R. Yi, I. Honma, J. Barber and V. Artero, *Nat. Mater.*, 2016, **15**, 640–646; (e) Q. T. Nguyen, P. D. Nguyen, D. N. Nguyen, Q. D. Truong, T. T. Kim Chi, T. T. D. Ung, I. Honma, N. Q. Liem and P. D. Tran, *ACS Appl. Mater. Interfaces*, 2018, **10**, 8659–8665.
- (a) B. Seo and S. H. Joo, *Nano Convergence*, 2017, **4**, 19; (b) B. Lassalle-Kaiser, D. Merki, H. Vrubel, S. Gul, V. K. Yachandra, X. Hu and J. Yano, *J. Am. Chem. Soc.*, 2015, **137**, 314–321; (c) F. Xi, P. Bogdanoff, K. Harbauer, P. Plate, C. Höhn, J. Rappich, B. Wang, X. Han, R. van de Krol and S. Fiechter, *ACS Catal.*, 2019, **9**, 2368–2380; (d) L. R. L. Ting, Y. Deng, L. Ma, Y.-J. Zhang, A. A. Peterson and B. S. Yeo, *ACS Catal.*, 2016, **6**, 861–867.
- (a) B. Hinnemann, P. G. Moses, J. Bonde, K. P. Jørgensen, J. H. Nielsen, S. Hørch, I. Chorkendorff and J. K. Nørskov, *J. Am. Chem. Soc.*, 2005, **127**, 5308–5309; (b) Q. Tang and D.-e. Jiang, *ACS Catal.*, 2016, **6**, 4953–4961.
- C. Tsai, H. Li, S. Park, J. Park, H. S. Han, J. K. Nørskov, X. Zheng and F. Abild-Pedersen, *Nat. Commun.*, 2017, **8**, 15113.
- (a) A.-Y. Lu, X. Yang, C.-C. Tseng, S. Min, S.-H. Lin, C.-L. Hsu, H. Li, H. Idriss, J.-L. Kuo, K.-W. Huang and L.-J. Li, *Small*, 2016, **12**, 5530–5537; (b) S. Li, S. Zhou, X. Wang, P. Tang, M. Pasta and J. H. Warner, *Mater. Today Energy*, 2019, **13**, 134–144.
- (a) D. Merki, H. Vrubel, L. Rovelli, S. Fierro and X. Hu, *Chem. Sci.*, 2012, **3**, 2515–2525; (b) C. T. Nguyen, T. A. Luu, T. D. Nguyen, A. T. Dam, L. T. Le, H. Han, S. T. Lo, P. T. Phan, H. T. Pham, H. N. T. Nguyen, L. L. Nguyen, H. Q. Nguyen and P. D. Tran, *ACS Appl. Mater. Interfaces*, 2023, **15**, 14215–14227.
- (a) X. Xu, H. Xu and D. Cheng, *Nanoscale*, 2019, **11**, 20228–20237; (b) D. Voiry, J. Yang and M. Chhowalla, *Adv. Mater.*, 2016, **28**, 6197–6206; (c) J. Zhang, T. Wang, P. Liu, S. Liu, R. Dong, X. Zhuang, M. Chen and X. Feng, *Energy Environ. Sci.*, 2016, **9**, 2789–2793.
- (a) W. Li, J. Liu and D. Zhao, *Nat. Rev. Mater.*, 2016, **1**, 16023; (b) H. Yu, H. Fan, J. Wang, Y. Zheng, Z. Dai, Y. Lu, J. Kong, X. Wang, Y. J. Kim, Q. Yan and J.-M. Lee, *Nanoscale*, 2017, **9**, 7260–7267.
- W. Li and D. Zhao, *Chem. Commun.*, 2013, **49**, 943–946.
- J. Kibsgaard, Z. Chen, B. N. Reinecke and T. F. Jaramillo, *Nat. Mater.*, 2012, **11**, 963–969.
- J. Deng, H. Li, S. Wang, D. Ding, M. Chen, C. Liu, Z. Tian, K. S. Novoselov, C. Ma, D. Deng and X. Bao, *Nat. Commun.*, 2017, **8**, 14430.
- A. Ambrosi and M. Pumera, *ACS Catal.*, 2016, **6**, 3985–3993.
- X. Chia and M. Pumera, *ACS Appl. Mater. Interfaces*, 2018, **10**, 4937–4945.
- L. Yang and Y. Ke, *High Perform. Polym.*, 2014, **26**, 900–905.
- T. M. Duong, P. D. Nguyen, A. D. Nguyen, L. T. Le, L. T. Nguyen, H. V. Pham and P. D. Tran, *Chem.–Eur. J.*, 2019, **25**, 13676–13682.
- L. Z. Kuangzhou Du, T. Wang, J. Zhuo, Z. Zhu, Y. Shao and M. Li, *ACS Appl. Mater. Interfaces*, 2017, **9**, 18675–18681.
- D. N. Nguyen, L. N. Nguyen, P. D. Nguyen, T. V. Thu, A. D. Nguyen and P. D. Tran, *J. Phys. Chem. C*, 2016, **120**, 28789–28794.



- 22 S. Homaeigohar, R. Kabir and M. Elbahri, *Sci. Rep.*, 2020, **10**, 5191.
- 23 J. Zhang, Z. Chen, Z. Wang, W. Zhang and N. Ming, *Mater. Lett.*, 2003, **57**, 4466–4470.
- 24 J. Luxa, V. Mazánek, D. Bouša, D. Sedmidubský, M. Pumera and Z. Sofer, *ChemElectroChem*, 2016, **3**, 565–571.
- 25 (a) X. Wang, B. Li, D. R. Bell, W. Li and R. Zhou, *J. Mater. Chem. A*, 2017, **5**, 23020–23027; (b) J. Chen, J. Cao, J. Zhou, Y. Zhang, M. Li, W. Wang, J. Liu and X. Liu, *Phys. Chem. Chem. Phys.*, 2020, **22**, 430–436; (c) L. Wang, Y. Hu, J. Lin, H. Leng, C. Sun, C. Wu, Q. Li and F. Pan, *J. Magnesium Alloys*, 2023, 2530–2540.
- 26 (a) V. Sánchez, E. Benavente, M. A. Santa Ana and G. González, *Chem. Mater.*, 1999, **11**, 2296–2298; (b) H. Vrubel, T. Moehl, M. Grätzel and X. Hu, *Chem. Commun.*, 2013, **49**, 8985–8987.
- 27 Z. Wu, B. Fang, Z. Wang, C. Wang, Z. Liu, F. Liu, W. Wang, A. Alfantazi, D. Wang and D. P. Wilkinson, *ACS Catal.*, 2013, **3**, 2101–2107.

